Weathering pulses during glacial-interglacial transitions: Insights from well-dated paleosols in the Azores volcanic province (Central North Atlantic)

Francisco Hevia-Cruz, Anthony Hildenbrand, Nathan Sheldon, Michael Hren, Vittorio Zanon, Fernando Marques, Julie Carlut, François Chabaux, Frédéric Haurine

Weathering pulses during glacial-interglacial transitions: insights from well-dated paleosols in the Azores volcanic province (Central North Atlantic)

Francisco Hevia-Cruz*[1], Anthony Hildenbrand[1], Nathan D. Sheldon[2], Michael T. Hren[3], Vittorio Zanon[4], Fernando O. Marques, Julie Carlut[5], François Chabaux[6], Frédéric Haurine[1]

[1]Université Paris-Saclay, CNRS, GEOPS, 91400 Orsay, France

[2]Department of Earth and Environmental Sciences, University of Michigan, USA

[3]Department of Earth Sciences, University of Connecticut, USA

[4]Instituto de Investigação em Vulcanologia e Avaliação de Riscos, Universidade dos Açores, Ponta Delgada, Portugal

[5]Université Paris Cité, Institut de physique du globe de Paris, CNRS, 75005 Paris, France

[6]Université de Strasbourg, CNRS, ITES (Institut Terre et Environnement de Strasbourg), 67084 Strasbourg Cedex, France

**corresponding author: francisco.hevia-cruz@universite-paris-saclay.fr*

Word count: 7908

Figure count: 4

Abstract

Volcanic islands evolve through complex interactions between volcano growth and surface processes. Climate changes impact the physical and chemical processes that drive weathering and denudation. While global paleoclimate has been extensively studied for the late Quaternary, elucidating the local climatic response to global forcing on such islands remains challenging. São Miguel is a volcanic island in the Eastern Azores, located in the Central North Atlantic, a region susceptible to changes in large-scale atmospheric and oceanic dynamics. It comprises numerous paleosols (PSs), whose geochemistry results from volcanic rocks' weathering and can serve as a proxy to reconstruct paleoclimatic conditions. New K-Ar and $^{40}Ar/^{39}Ar$ ages of volcanic units "bracketing" (under and overlying) PSs reveal four periods of enhanced soil formation (~820–765 ka, ~425–430 ka, ~170–75 ka, <10 ka), coinciding with rapid glacial-interglacial transitions (Terminations I, II, V, IX). Our reconstructed mean annual precipitation (MAP; 500–1200 mm yr^{-1}) and air temperature (MAAT; 12–18 °C) are higher during interglacial peaks. This, in addition to the coherence of MAAT with previous Sea Surface Temperature reconstructions, shows consistency between local and global climate dynamics. The texture of parental rocks played a significant role in weathering, with PSs predominantly restricted to the brecciated upper part of lava flows and to pyroclastic deposits, which exhibited distinctive precipitation thresholds for their formation (~800 mm yr^{-1} and ~500 mm yr^{-1}, respectively). PSs developed on basaltic lava flows exhibit greater elemental loss, due to a high glass proportion and low permeability, which prevents fluids percolation out of the soils. As present-day precipitation and temperature exceed those of the past, enhanced weathering is expected in São Miguel and other volcanic islands, with local to global impacts (e.g., carbon cycling), especially in the context of ongoing global warming.

Keywords: paleoclimate, Ar geochronology, geochemistry, pedogenesis, Atlantic Ocean

1. Introduction

Climate changes impact landscape evolution on volcanic islands in a variety of ways. Cold and dry glacial periods may favor canyon deepening and coastal erosion as a result of low eustatic sea level (e.g., Hildenbrand et al., 2008a). Conversely, wetter and warmer conditions during fast glacial-interglacial transitions likely increase rock weathering and soil formation (Kramer & Chadwick, 2016), thus favoring subsequent denudation. While global climate can be studied through direct observations during historical times and through different proxies for most of the Quaternary (e.g., δD in ice cores, foraminifera $\delta^{18}O$ in marine sediment cores, eolian dust mass accumulation), it remains challenging to constrain the magnitude and rate of the local climatic response to global forcing at these time scales (Menviel et al., 2020).

The Azores, located in the Central North Atlantic (Figure 1), represent a unique site to study the paleoclimatic evolution of volcanic islands. The local climate is influenced by large-scale drivers, such as the North Atlantic High Pressure System, also known as Azores High, and the divergence of the Gulf Stream into the North Atlantic and Canary Currents. Thus, the Azores also represent a key opportunity to study the evolution of the North Atlantic hydroclimate. In particular, São Miguel Island has been volcanically active throughout the last one million years (Myr) and includes periods of volcanic quiescence, sometimes represented by paleosols (PSs; Figures 1 to 3). Paleosol formation processes, as recorded by their geochemistry, directly reflect the environmental conditions in which they formed, making it possible to reconstruct past precipitation and temperature (Sheldon & Tabor, 2009). Among the factors that control soil formation (parental material, climate, topography, organic activity, time), climate is one of the most relevant (White, 2005), as organic activity is susceptible to climatic conditions and in the relatively flat lowlands of volcanic islands, topography should not play a major role. In addition, several studies point to fast weathering during the first few thousand years of soil formation, which tends to equilibrium due to precipitation of stable clay minerals in the soil and cations depletion of the weathered rock (Rad et al., 2011, 2013; Sowards et al., 2018; Böker et al., 2019; Chadwick et al., 2022). In the case of

paleosols developed in pyroclastic deposits, pedogenesis can take place as fast as centennial to millennial scale (e.g., Solleiro-Rebolledo et al., 2015). At geological time scales (> 1 Ma), this is a fast process (< 100 kyr). Thereby, PS's geochemistry reflects actual average atmospheric conditions at the time of soil formation. In consequence, it has been used as a paleoclimatic proxy in different volcanic contexts, such as the western USA, south-eastern Iberian Ranges, and the Lower-Upper Cretaceous Rukwa Rift Basin in Tanzania (Sheldon 2006b; de la Horra et al.; 2012; Orr et al., 2021). Additionally, high accumulation rates of volcanic products and the intercalation of PSs among them allow for precise determination of both PS age and the duration of soil formation, in contrast with most non-marine records. Other terrestrial records, such as tree rings and carbonates, also allow for paleoclimatic reconstructions, but are generally restricted to the Holocene (e.g., Steinhilber et al., 2012; Thatcher et al., 2020).

Here we present a combined geochemical and geochronological study of PSs spanning the last 1 Myr in São Miguel Island. We aim to reconstruct the local paleoclimatic response to global climatic forcing, and to understand the climatic impact on weathering and landscape evolution.

2. General setting

The Azores Archipelago is located in the central North Atlantic Ocean, near the triple junction of North America, Eurasia, and Nubia lithospheric plates (Figure 1A). It is made up of nine volcanic islands spread over ~600 km in a WNW-ESE trend and distributed in three groups: The Western Azores (Flores and Corvo islands), the Central Azores (São Jorge, Pico, Faial, Graciosa and Terceira islands), and the Eastern Azores (Santa Maria and São Miguel islands). The climate of the archipelago is influenced by the Azores Current, an ESE branch of the North Atlantic gyre that turns southward into the Canary Current, and the North Atlantic High Pressure, also known as the Azores High (Klein & Siedler, 1989; Rashid et al., 2012; Cresswell-Clay et al., 2022). In São Miguel's coastal areas, the average annual air temperature ranges between 14 and

18 °C, and at high-altitude internal sites, between 6 and 12 °C (AEMET & IM, 2012). Mean annual precipitation ranges between ~450 and 1450 mm yr^{-1} in Ponta Delgada, the main town of the island, reaching over 3000 mm yr^{-1} in the highest eastern summits (Pico da Vara, 1103 m a.s.l.; AEMET & IM, 2012; Hernández et al., 2016). There are four Köppen-Geiger climatic zones (Köppen, 1936): temperate with no dry season with mild summer (Cfb) for most of the island, temperate with dry-warm summer (Csb) for low relief zones, temperate with no dry season and with hot summer (Cfa) for a restricted area of the north shore, and temperate with hot-dry summer (Csa) for some coastal areas (Figure 1B).

São Miguel Island has grown along the Terceira Rift (TR), a hyper-slow oceanic rift making up the eastern boundary between Eurasia and Nubia tectonic plates (Marques et al., 2013). The island has been volcanically active throughout the last 1 Myr, and was progressively built by a general westward displacement of volcanic activity into historic times. Based upon K-Ar geochronology of groundmass and alkali feldspar separates, Sibrant et al. (2015) described six constructional phases that include both effusive and explosive activity, as well as periods of relative volcanic quiescence. The oldest volcano (Nordeste Complex), making up the eastern end of the island, experienced dominant sub-aerial growth between 880 ka and 750 ka (purple unit in Figure 1B). After a major S-directed collapse of the volcano's former flank, the collapse depression was massively buried by basic to intermediate lava flows between 507 ka and 250 ka (blue unit in Figure 1B).

Subsequent volcanic activity was mostly concentrated in the central and western parts, through the growth and partial destruction of three main central volcanoes, which are, from east to west: Furnas, Fogo and Sete Cidades (green, yellow and red units in Figure 1B, respectively). These were the locus of alternating effusive and explosive activity, producing several major pyroclastic flows and tephra layers of dominant trachytic composition, associated with multiple caldera collapses (e.g., Sibrant et al., 2015). Finally, numerous scoria cones and associated basic lava flows developed between the three main central edifices, producing linear NW-SE to E-W

123 oriented “Waist Zones”. Further details about eruption ages and their relationship with the
124 tectonics of the TR can be found in Sibrant et al. (2015, 2016).

125 During volcanic quiescence periods, soils were developed on different volcanic deposits
126 (e.g., Figures 2, 3), and were incorporated into the geological record as PSs. The high variability
127 of volcanic rocks in São Miguel Island makes it possible to study the influence of different
128 compositions and textures on soil formation and to assess the respective contributions of
129 geological and paleoclimatic controls on weathering processes.

130

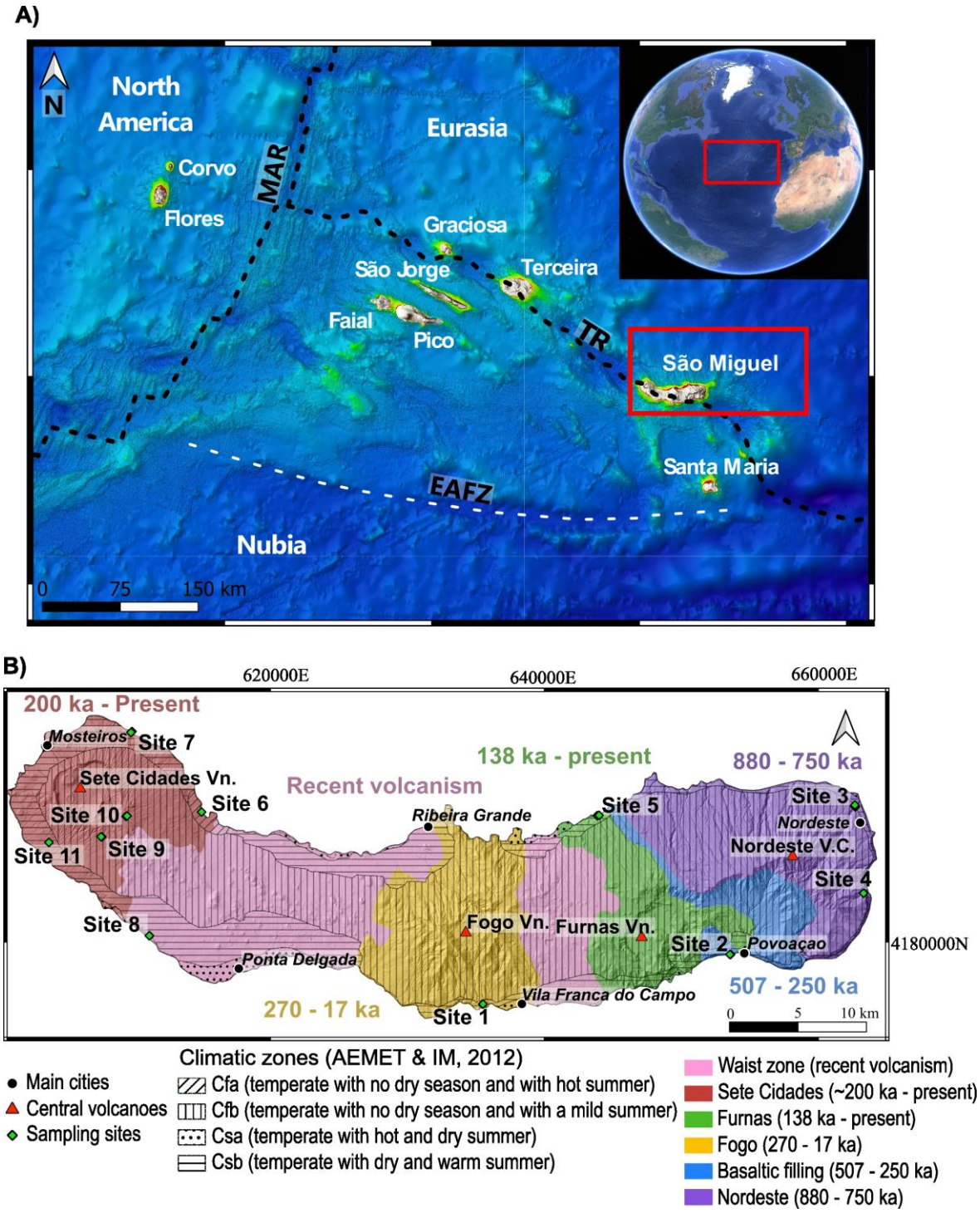

Figure 1: *São Miguel Island's physiographic setting. A) Location of São Miguel Island at the eastern end of the Azores Archipelago and its tectonic context. MAR: Mid Atlantic Ridge; EAFZ: East Azores Fracture Zone; TR: Terceira Rift. B) Main volcanic units of São Miguel Island (color*

code) after Sibrant et al. (2015) and references therein. Climatic zones distribution after Köppen-Geiger (after Köppen, 1936; AEMET & IM, 2012).

3. Methods

3.1. Fieldwork and sampling strategy

We conducted two fieldwork campaigns to São Miguel Island in September 2021 and May-June 2022. The visited sites concentrate on coastal cliffs and road cuts in the western and eastern parts of the island, where volcanic successions are better exposed (Figure 1B).

Based upon observations of previous fieldwork campaigns, we targeted paleosol profiles without evident recent diagenetic alteration or polygenetic mixing, and preferentially studied those intercalated between well-preserved volcanic deposits (Figure 2) to precisely bracket the timing and rate of PS formation. In total, 14 fresh cores of massive lava flows were sampled for K-Ar dating on groundmass separates, and four alkali feldspar-rich pyroclastic deposits were selected for $^{40}Ar/^{39}Ar$ dating (Figures 2, 3; Tables 1, 2). Special care was taken in the field to avoid weathered lava flows. Our PS age constraints further include 12 previously published ages, six obtained by K-Ar on groundmass separates (Sibrant et al., 2015; Ricci et al., 2020), and six by radiocarbon on organic matter of PSs for the deposits younger than 10 ka (Conte et al., 2019).

Paleosols were classified according to the USDA soil taxonomy (Soil Survey Staff, 2014) and Mack et al. (1993) classification systems, based on their physical characteristics. We made field observations of the number of horizons and their thicknesses, color, contact morphology and parent rock composition, as well as their reaction to 10% HCl to evaluate the presence of carbonates. Each recognized horizon, including the unweathered volcanic parental rock, was sampled for geochemical analyses. The upper part of PSs that were reworked by overriding lava flows were discarded to avoid the incorporation of potentially thermally-altered materials. For those PS profiles without alteration observed in the field, at least 10 cm of the surface was

161 removed before sampling to avoid contamination from recent weathering processes. The number
162 and depth of samples were variable, depending on the horizon's thickness and vertical variations,
163 between two for the thinner PS and eleven for a composite PS, but generally between four and
164 six, separated by ~5–10 cm (Figure 3C). Three PSs were re-sampled in the 2022 field campaign
165 to evaluate the reproducibility of our sampling and analyses. Munsell color was recorded in the
166 laboratory on dry samples. All profile and sampling information is included in Supplementary Table
167 ST1.
168
169 **3.2. Geochronology**
170
171 **3.2.1. Unspiked K-Ar**
172 The unspiked K-Ar Cassignol–Gillot technique (Gillot and Cornette, 1986) has a large
173 applicable age range, and has been successfully and widely used to date low K content lavas in
174 different volcanic settings, including the Azores archipelago (Hildenbrand et al. 2008b, 2012,
175 2014, 2018; Sibrant et al, 2015; Marques et al., 2018, among others). Relative uncertainty is
176 defined as the square root of the sum of three factors: the K measurement uncertainty (~1%), ^{40}Ar
177 signal calibration (~1%), and the uncertainty on the atmospheric calibration correction, which
178 rapidly becomes negligible for samples with more than 10% of radiogenic Argon. As a result,
179 typical uncertainties are ~1.5% or as low as a few ka for lavas older than ~100 ka (e.g., Sibrant et
180 al., 2015; Hildenbrand et al., 2018; Quidelleur et al., 2022), which encompasses most of São
181 Miguel's volcanic activity.
182 After thin section examination, lava samples were crushed and sieved to the 125–250 μm
183 size fraction and washed with nitric acid at 10% concentration in an ultrasonic bath. The
184 groundmass was then isolated by heavy liquids and magnetic separation. As it formed during lava
185 flow cooling, it is representative of eruption age. Phenocrysts were systematically discarded, as
186 they may have formed earlier at depth (pre-eruptive crystallization), yielding abnormal "too-old"

ages by unsuitable incorporation of potentially inherited excess-argon (Gillot et al., 2006). Most samples had low content of volcanic glass, and no important devitrification was observed in thin sections. Denser fractions of groundmass were preferred, as devitrified materials are less dense due to clay precipitation, ensuring to avoid weathered materials.

K concentration was measured by atomic absorption with an Agilent 240 AA spectrometer. For each sample, the K average value (Table 1) was obtained from at least two independent measurements on distinct aliquots. The uncertainty on K determination is typically less than 1% (1σ), as deduced from sample reproducibility and from measurements of standards treated under the same conditions (MDO-G and BCR-2, after Gillot et al. (1992) and Wilson (1997), respectively). Independent argon measurements were performed using a magnetic sector mass spectrometer with simultaneous collection of ^{40}Ar and ^{36}Ar on Faraday cups. Measurement of the Ar atmospheric contamination was determined from pure air analyzed under the same pressure as the samples by means of adjustable volumes. Stable and high vacuum measurement conditions allow the detection of tiny (<0.1 %) amounts of radiogenic $^{40}Ar^{*}$. Periodic measurements of standard HD-B1 were carried out for quality control and $^{40}Ar^{*}$ calibration, with a recommended age of 24.18 ± 0.09 Ma (Schwarz & Trieloff, 2007) calculated following Renne et al. (1998) recommended values for commonly used standards. Further details on the analytical procedure and age uncertainty calculation can be found elsewhere (Gillot et al., 2006; Hildenbrand et al., 2018).

3.2.2. $^{40}Ar/^{39}Ar$ geochronology

Pumices from four pyroclastic deposits were crushed and sieved (500 µm to 1 mm fraction, except sample SM21M4 of site 8, in the 250 µm to 1 mm fraction), and unaltered alkali feldspar phenocrysts were handpicked under a binocular microscope. The crystals were leached for 3 minutes in a 5% HF acid solution in an ultrasonic bath to remove any attached groundmass, and then rinsed with distilled water.

The crystals were irradiated for 2 hours in the Cd-lined in-core CLICIT facility (OSU TRIGA reactor; details of sample irradiation and analyses are provided as electronic supplementary material). Twenty irradiated crystals per sample were mounted in a copper holder, connected to the extraction line and underwent 10 s sweeping under high-vacuum at 0.2 W to eliminate atmospheric contamination. Each crystal was fused individually and the extracted gas was purified with a cold getter (90 s) and two hot getters (210 s), and transferred to an NGX600 mass spectrometer by pressure equilibrium. The ^{40}Ar, ^{39}Ar, and ^{38}Ar isotopes were measured in an array of 9 ATONA Faraday cups, while ^{36}Ar and ^{37}Ar were measured in an electron multiplier with a gain set at 1.31. A blank was measured between every two crystals, with typical measurements of $1.7\ 10^{-4}$V to $2.0\ 10^{-4}$V for ^{40}Ar and 65 cps for ^{36}Ar ($9.5\ 10^{-7}$ V equivalent). Data reduction was achieved using ArArCALC V2.4 (Koppers, 2002), and the J-value (0.0005619 ± 0.00000045, 1σ) was determined from co-irradiated Alder Creek Rhyolite sanidine ACs-2 with a recommended age of 1.1891 ± 0.0008 Ma (Niespolo et al., 2017). Air pipettes were measured overnight to monitor the mass discrimination with a $^{40}Ar/^{36}Ar$ ratio of 298.56 (Lee et al., 2006). This technique is particularly useful for precisely dating single-grain alkali feldspars at the temporal scale of São Miguel Island (a few ka to ~1 Ma), discriminating inherited phenocrysts. Typical uncertainties are lower than 1% or just a few thousand years (e.g., Pereira et al., 2020; Monaco et al., 2022). Further details about the analytical procedure and data reduction can be found elsewhere (e.g., Giaccio et al., 2021, and references therein).

3.3. Paleosol geochemistry

Based on geochronological constraints, 84 samples from 18 PSs were selected for geochemical analyses. They were dried in an oven at 60 °C for 3 to 4 days and an aliquot of the bulk sample was crushed with an agate pestle and mortar, and then powdered in a Retsch PM-200 planetary agate mill. Major element analyses were made in an iCap6500 ICP-OES (SARM laboratory, France; uncertainties in Supplementary Table ST2), and trace element analyses were

made in a ThermoScientific Element XR-HR-ICP-MS (GEOPS laboratory, France) after acid digestion and dilution. Trace elements measured on standard samples (BCR-2, BHVO-2, BXN, JSd-1, SL-1) were within certified expected ranges (Supplementary Table ST2). Additionally, 136 sample powders (including replicates; 40 mg) were loaded in tin capsules for C and N concentration measurements in a Costech ECS4010 elemental combustion system (GRiTS laboratory, Earth and Environmental Sciences Department of the University of Michigan), and 35 more (35 mg) for $\delta^{13}C$ measurements by a Costech ECS4010 elemental analyzer coupled to a MAT253 isotope-ratio mass spectrometer (IRMS) via continuous flow at the University of Connecticut. Analytical precision for carbon and nitrogen concentrations was better than 0.3 wt%, and analytical precision for IRMS measurements was better than 0.1‰.

Mass transfer function of a mobile element "j" in sample "w" relative to an immobile element "i" in parental rock "p" was made by calculating mass changes (τ) as a function of immobile elements (ε) following Chadwick et al. (1990):

$$\tau_{j,w} = \frac{\rho_w C_{j,w}}{\rho_p C_{j,p}} \left(\varepsilon_{i,w} + 1\right) - 1$$

with $C_{j,w}$ the concentration of j in sample w, $C_{j,p}$ the concentration of element j in the parental rock, ρ_p the density of the parental rock, ρ_w the density of the sample, and $\varepsilon_{i,w}$ the strain or volumetric variation of an immobile element i in sample w, relative to the bed rock:

$$\varepsilon_{i,w} = \frac{\rho_p C_{i,p}}{\rho_w C_{i,w}} - 1$$

where $C_{i,p}$ is the concentration of an immobile element i in the parental rock and $C_{i,w}$ the concentration of an immobile element i in sample w. Combining (a) and (b), we get:

$$\tau_{j,w} = \frac{C_{j,w} C_{i,p}}{C_{j,p} C_{i,w}} - 1$$

where $\tau_{j,w}$ is the mass fraction of element j added to the system during weathering relative to the same element in the parental material.

Sample density was estimated based on past work (Rosi et al., 1999; Moore, 2001; Sheldon & Retallack, 2001; Polacci et al., 2003; Carmichael, 2017), and potential diagenetic additions of alkali elements were evaluated following Sheldon (2003, 2006b).

3.3.1. Paleoenvironmental reconstructions

Whole-rock geochemical analyses of B horizons (weathered clay-enriched horizons with respect to A, C and R horizons due to illuviation) were used to calculate PS weathering indices: (1) Chemical Index of Alteration Minus Potash (CIA-K = $100x[Al_2O_3/(Al_2O_3+CaO+Na_2O)]$; Maynard, 1992) and (2) Clayeyness Index ($C = Al_2O_3/SiO_2$; Retallack, 2001). Those results were then used with geochemical climofunctions derived from modern soils to reconstruct mean annual precipitation (MAP) and mean annual air temperature (MAAT) as follows:

(1) $$MAP = 221.12e^{0.0197(CIA-K)}$$

with $R^2 = 0.72$ and a standard error of ± 181 mm yr^{-1} (Sheldon et al., 2002), and

(2) $$MAAT = 46.9C + 4$$

with $R^2 = 0.96$ and a standard error of ± 0.6 °C (Sheldon, 2006a), and where total error is typically assigned as 3 times the standard error (±2 °C; Sheldon and Tabor, 2009). Sheldon et al. (2002) used CIA-K because K is more susceptible to being affected by organic activity. The data used by them and by Sheldon (2006a) comes from a US government soil survey by Marbut (1935) that includes soils from virtually every US state or territory (e.g., Puerto Rico) and thus spans most of the range of climate-space on Earth today, except for tundra soils. Soil formation times in that dataset range from 1 kyr up to 100 kyr, so all of the PSs in this study are bracketed by age constraints of the training data. Summary data tables are published as supplemental information by Sheldon et al. (2002). Those authors considered that the chemistry of the soils is in equilibrium with the atmospheric conditions, as they did not observe a clear relationship between the age of the soils and the weathering degree in 10^3–10^5 yr temporal scales, thus they did not include the time as a variable. Elemental concentrations were used as molecular ratios (oxide weight percent

288 divided by their molecular weight). B horizons are used because their long formation times result
289 in chemistry that is a function of equilibrium processes, and also avoids short-term climatic
290 variations (Sheldon and Tabor, 2009). Both climofunctions have previously been used in volcanic
291 settings (e.g., Sheldon, 2003, 2006a; de la Horra, 2012; Orr et al., 2021) and were comparable to
292 independent estimates from both inorganic and plant-based proxies.
293
294 **4. Results**
295
296 **4.1. Timing of paleosol formation**
297 The age and duration of PS formation are constrained by 18 new ages and 12 previously
298 published ages. Note that the calibrations for K-Ar and $^{40}Ar/^{39}Ar$ are different, but the associated
299 age bias is minor. Indeed, the standard HD-B1 has an age of 24.18 Ma relative to GA-1550 at
300 98.79 Ma in Schwartz and Trieloff (2007). As ACs is dated at 1.194 Ma relative to GA-1550 at
301 98.79 Ma in Renne et al. (1998), the age of HD-B1 at 24.18 Ma we are using here for K-Ar
302 calibration is fully compatible with the age of 1.1891 Ma (Niespolo et al., 2017) used here for the
303 $^{40}Ar/^{39}Ar$ calibration. Effectively, the two ages reported above for ACs agree within a few ‰. In our
304 case, this yields age differences of less than 0.5 ka for paleosols formed around 100 ka, and a
305 couple of kyr for paleosols older than 500 kyr. Such differences are lower than typical age
306 uncertainties and have a negligible impact on paleoclimatic interpretations.
307 Our new K-Ar ages (n = 14) range between 84 ± 2 ka and 822 ± 12 ka (Table 1), whereas
308 our four new $^{40}Ar/^{39}Ar$ ages vary between 71.0 ± 0.5 ka and 429.4 ± 1.4 ka (Table 2,
309 Supplementary Figure SF1). These results are consistent with previous K/Ar and $^{40}Ar/^{39}Ar$
310 determinations on separated phases acquired on the main units of the island (e.g., Johnson et al.,
311 1998; Sibrant et al., 2015; Ricci et al., 2020; and references therein). The new K/Ar and $^{40}Ar/^{39}Ar$
312 ages obtained on volcanic deposits bracketing individual paleosols are highly consistent. All of
313 them match the available stratigraphic control and most of them overlap within uncertainties.

Sample	Site	UTM N	UTM E	K%	40Ar*%	40Ar* (10^{11} at/g)	Age [ka]	1σ [ka]
SM21AA12	8	4180461	611157	1.882	4.2	1.66	85	2
				1.882	3.9	1.64	83	2
						Mean	**84**	**2**
SMi16B	7	4195345	609871	2.669	10.7	3.64	131	2
				2.669	10.1	3.60	129	2
						Mean	**130**	**2**
SM21X	7	4195315	609813	3.051	15.9	4.40	138	2
				3.051	15.0	4.38	137	2
						Mean	**138**	**2**
SM22G	8	4180221	611450	0.330	1.4	0.48	140	10
				0.330	1.4	0.49	142	10
						Mean	**141**	**10**
SMi16A	7	4195403	609922	2.273	10.7	4.85	204	3
				2.273	12.0	4.80	202	3
						Mean	**203**	**3**
SM22A	2	4179080	653546	3.325	24.4	14.92	430	6
				3.325	25.1	14.61	421	6
						Mean	**425**	**6**
SM22B	2	4179102	653607	3.505	44.4	15.60	426	6
				3.505	47.7	15.55	425	6
						Mean	**425**	**6**
SMi16H	5	4189184	643713	2.067	30.9	9.18	425	6
				2.067	35.5	9.27	429	6
						Mean	**428**	**6**
SMi16I	5	4189293	643993	2.111	38.0	9.40	426	6
				2.111	39.4	9.52	432	6
						Mean	**429**	**6**
SMI16J	5	4189293	643993	2.549	18.5	11.62	437	7
				2.549	28.4	11.49	432	6
						Mean	**434**	**6**
22SM11	3	4189943	662672	2.029	49.5	16.37	772	11
				2.029	48.0	16.54	780	11
						Mean	**776**	**11**
22SM10	3	4189889	662693	1.489	33.6	12.26	788	11
				1.489	33.4	12.24	787	11
						Mean	**788**	**11**
SM22D	4	4183502	663289	1.818	50.9	15.66	825	12
				1.818	54.8	15.51	817	12
						Mean	**821**	**12**
SM22F	4	4183564	663315	1.749	57.2	15.09	826	12
				1.749	60.4	14.94	817	12
						Mean	**822**	**12**

Table 1: *New K-Ar ages obtained in groundmass separates. Sampling sites shown in Figure 1B. All ages are reported at 1σ confidence level. Decay constants and isotopic ratios from Steiger and Jäger (1977). Reported K values are the average of at least two independent measurements on distinct sample aliquots. Projection Zone 26S (WGS 84).*

The K/Ca ratios of sample SM21M4's crystals (site 8) were very low (< 1%), and only 7 of the 20 feldspar phenocrysts could be dated as a consequence of the low signals, with an associated error of 10 ka (Table 2, Supplementary Figure SF1). Nevertheless, this age is still consistent with the stratigraphy of the island, and is reinforced by a K-Ar age of 141 ± 10 ka on the lava flow SM22G (site 8), which underlies SM21M4 (site 8; Tables 1, 2). Older inherited phenocrysts were discarded for the preferred ages of samples SM21C2 (site 1), SM21T3 (site 6) and SM21G4 (Site 2; Supplementary Figure SF1).

Sample	Site	UTM N	UTM E	Weighted mean age ± 1σ [ka]	MSWD	Summed total gas age ± 1σ [ka]	Normal isochron age ± 1σ [ka]	Inverse isochron age ± 1σ [ka]	$^{40}Ar/^{39}Ar$ intercept	Mean K/Ca ratio ± 1σ	**Preferred age ± 1σ [ka]**
SM21C2	1	4175436	635525	71.0 ± 0.4	0.67	71.7 ± 0.5	72.8 ± 0.7	71.0 ± 0.7	298.1 ± 5.4	8.1 ± 0.1	**71.0 ± 0.5**
SM21T3	6	4189501	614971	79.0 ± 0.5	1.1	82.1 ± 0.5	78.7 ± 0.8	79.2 ± 0.8	298.0 ± 2.0	14.5 ± 1.4	**79.0 ± 0.5**
*SM21M4	8	4180431	611177	139.0 ± 9.8	0.118	138.7 ± 11.3	145.3 ± 16.0	145.5 ± 15.9	296.0 ± 5.0	0.047 ± 0.006	**139.2 ± 9.8**
SM21G4	2	4179083	653579	429.4 ± 0.9	0.86	436.7 ± 2.0	435.2 ± 1.9	429.2 ± 1.0	298.9 ± 0.6	7.0 ± 0.5	**429.4 ± 1.4**

Table 2: *New $^{40}Ar/^{39}Ar$ ages obtained on alkali feldspar crystals. Preferred ages are reported at 1σ confidence level, considering the full external error. Decay constants after Renne et al. (2011). Projection Zone 26S (WGS 84). Sampling sites of Figure 1B. (*) Indicative age on plagioclase crystals, as only crystals with high enough K/Ca ratios (> 0.03) could be analyzed.*

Twelve available published ages and our new geochronological data allowed us to constrain PS ages in four clusters: ~820–765 ka, ~425–430 ka, ~170–75 ka, and <10 ka (Figure 4, Supplementary Table ST1). The two older groups are better constrained in time, and show maximum soil formation time of only a few thousand years. In each case, the volcanic unit overlying a PS provides its minimum age, whereas the volcanic unit underlying the PS provides its maximum age. The age of the PS was considered as the average of both, and the maximum PS formation time as the difference between the maximum age plus its uncertainty minus the minimum age minus its uncertainty (Figure 2). As the ^{14}C ages reported by Conte et al. (2019) correspond to organic matter, the respective PSs do not count with a minimum PS age and, consequently, no PS maximum formation time was estimated for those cases.

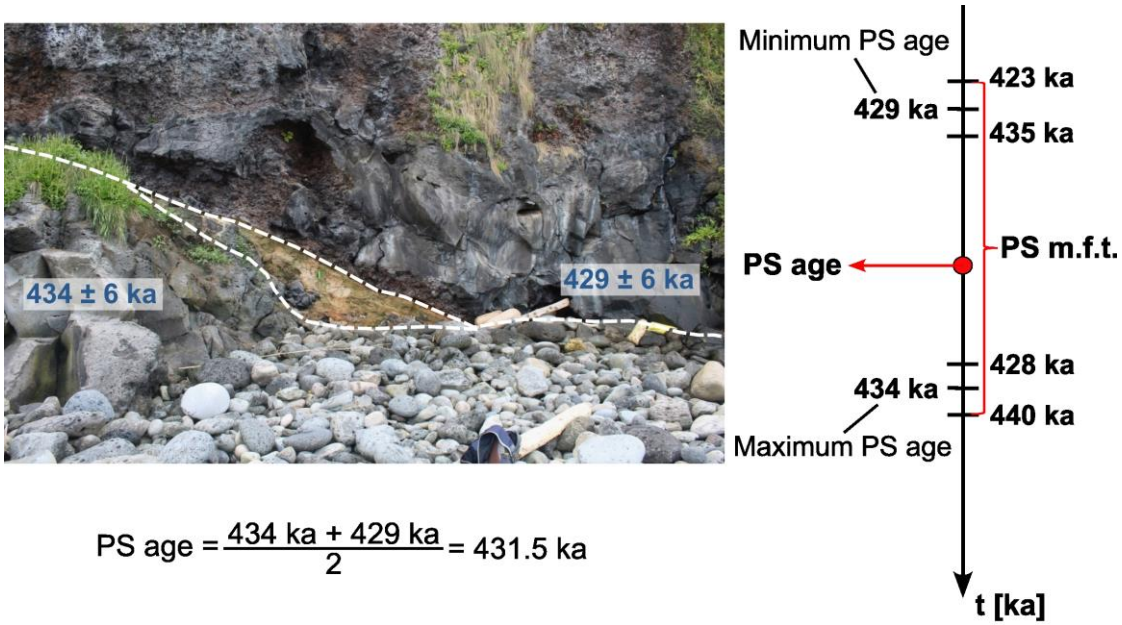

$$\text{PS age} = \frac{434\ \text{ka} + 429\ \text{ka}}{2} = 431.5\ \text{ka}$$

PS m.f.t. = PS maximum formation time = (434 ka + 6 ka) - (429 ka - 6 ka) = 17 ka

Figure 2: *Example of a paleosol geochronological constraint. The lava flows dated at 429 ± 6 ka and 434 ± 6 ka give the minimum and maximum age of the PS, respectively.*

4.2. Paleosol characterization

4.2.1. Paleosol physical characteristics

All of the PSs are classified as Inceptisols and Andisols according to the USDA soil taxonomy classification system (Soil Survey Staff, 2014). They were developed on diverse parental volcanic rocks, ranging from mafic lava flows and Strombolian tephra deposits to trachytic pumice-bearing fallout deposits (Type I, II and III in Figure 3A, 3B and 3C, respectively). All the studied PSs exhibit a clear horizonation but lack further features to be classified as more developed soils (Fig. 3A-C, Supplementary Table ST1). Consequently, according to the paleosol-specific classification system of Mack et al. (1993), they all correspond to Protosols. Their thicknesses range between ~15 cm and ~115 cm (without considering R horizons), with two exceptions: a ~3 m thick composite PS and a very thin (~3 cm-thick) PS. The observed PSs typically vary from light grayish brown (7.5YR6/2), mainly those developed in felsic pyroclastic deposits, to yellowish (7.5YR6/6) and red (10R4/6) for those developed in lava flows and mafic Strombolian deposits. No carbonate was observed. For most profiles, A horizons are not preserved or are incompletely preserved, and the typical horizonation is Bw-C-R or Bt-C-R (colored B horizon (Bw) with illuviated clay accumulation (Bt) - weathered parental rock (C) - fresh parental rock (R)). According to the classification of Milne et al. (1995), contacts between horizons are smooth to wavy and distinct to diffuse, except for the contacts of PSs developed on lava flows, for which basal contacts with the parental rock are wavy to irregular and sharp. Detailed features and descriptions of each PS profile can be found in Supplemental Table ST1.

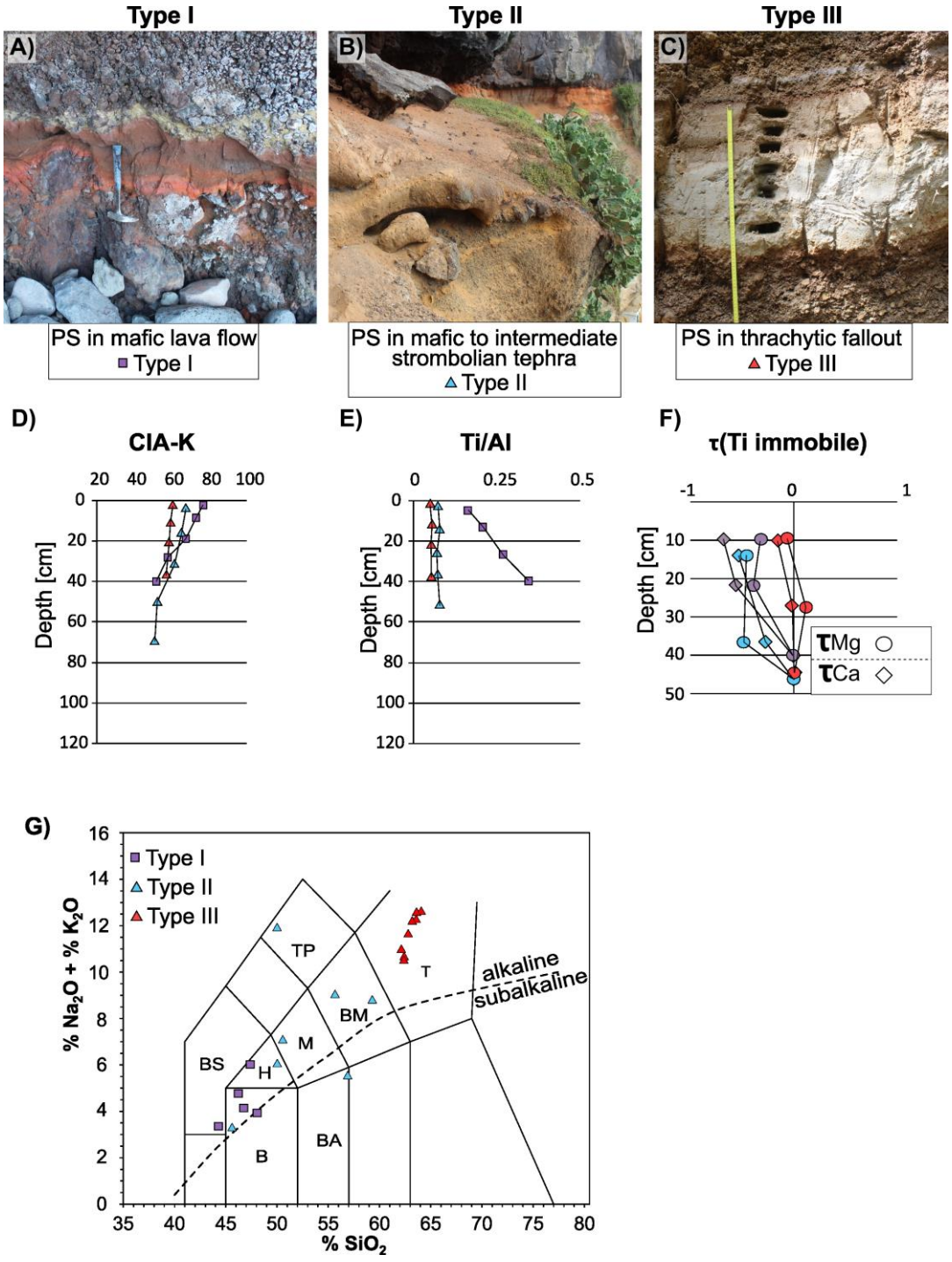

367

368 ***Figure 3:*** *Paleosols developed on different types of parental materials. A) Type I PS, developed*
369 *in the brecciated upper part of a basaltic lava flow (purple-colored square); B) Type II PS,*
370 *developed in a coarse basaltic pyroclastic deposit (light blue triangle); C) Type III PS, developed*
371 *in a fine trachytic ash-fall deposit (red triangle); D) Mean CIA-K variations by PS type; E) Mean*

Ti/Al ratios by PS type; F) Mean Ca and Mg loss by PS type (circles for Mg; diamonds for Ca; colors as in A, B and C); G) TAS diagram of the parental rock by PS type. B: basalt, BA: basaltic andesite, BS: basanite, H: hawaiite, M: mugearite, BM: benmoerite, TP: tephriphonolite, T: trachyte, field names after Le Bas et al. (1986). In F), Negative Tau (τ) values indicate relative elemental loss and positive values indicate relative elemental gain. The values and variations in D), E) and F) graphics represent the main tendencies by PS type and not individual profile values. Full CIA-K, Ti/Al and Tau (τ) values are available in Supplementary Figure SF2.

4.2.2. Paleosol geochemistry

The chemical compositions of the parental rocks of PSs are variable and form an alkaline series from basalt and basanite to trachyte (Figure 3G). The PSs of the Nordeste Volcanic Complex were developed on three basalts and a basanite; those of Povoaçao are on a hawaiite, on a basaltic-andesitic and two benmoreitic pyroclastic deposits; the two PSs of Fogo volcano are on trachytic pyroclastic deposits; and most of Sete Cidades Volcano's pyroclastic rocks are trachytic, but range from basaltic to trachytic (Figure 3G).

The elemental composition of individual PS profiles shows significant variations from almost 100% loss to over 1000% gain, relative to parental rocks, which is much greater than the analytical uncertainties (Supplementary Figure SF2). Full geochemical data are shown in Supplementary Tables ST3 (major and trace elements).

Most of the profiles have an upward increase in weathering indices (Figure 3D), mostly controlled by Ca and Mg loss, and by Al, Si and Fe accumulation relative to parental material (Figure 3F, Supplementary Figure SF2). Type I PSs have the greater CIA-K increase, generally from ~40 to ~70. Type III PSs show modestly increasing CIA-K values, generally between 56 and 60, and type II are intermediate between types I and III (generally between 45 and 65, Figure 3D), with one exception that reached 85 (Supplementary Figure SF2).

Most types II and III PSs have fairly constant Ti/Al ratios (< 20% difference, Figure 3E), while most type I PSs have an up-profile decrease (~45% to ~80% difference, Figure 3E) and two of them an increase (8% and 44%, Figure 3E), although their La/Ce ratios are much constant (~15 to ~43% difference, Supplementary Figure SF2).

4.3. Paleoclimatic reconstruction

Using eq. 1–2, MAP and MAAT were reconstructed as ranging from 518 to 1194 mm yr^{-1} and 11.8 to 18.2 °C (Figure 4, Supplementary Table ST3), with mean values of 790 mm yr^{-1} and 14.5 °C, respectively. Those variations are significant, considering the standard errors of the proxies (182 mm and 2 °C, respectively). A general decline of MAAT is observed for the last 820 ka, with relatively steadier MAP, and with higher variability for the two intermediate age groups (Figure 4; e.g., the 425–430 ka group). Calculated MAP and MAAT are lower than the present-day values of 1052 mm yr^{-1} and 17.8 °C at Ponta Delgada (AEMET & IM, 2012; Hernández et al., 2016), except for one paleosol that reaches 1194 ± 182 mm yr^{-1} and 18.2 ± 2 °C at ~430 ka (SM22J in site 5, northern shore of the island, Figure 1B, Supplementary Table ST3).

Both the N and C contents are typically <0.5% (Supplementary Table ST4). The $\delta^{13}C$ values range between -31.15‰ and -22.90‰, with a mean value of -25.42‰, and show a slight decrease over the last ~820 ka (Supplementary Table ST5).

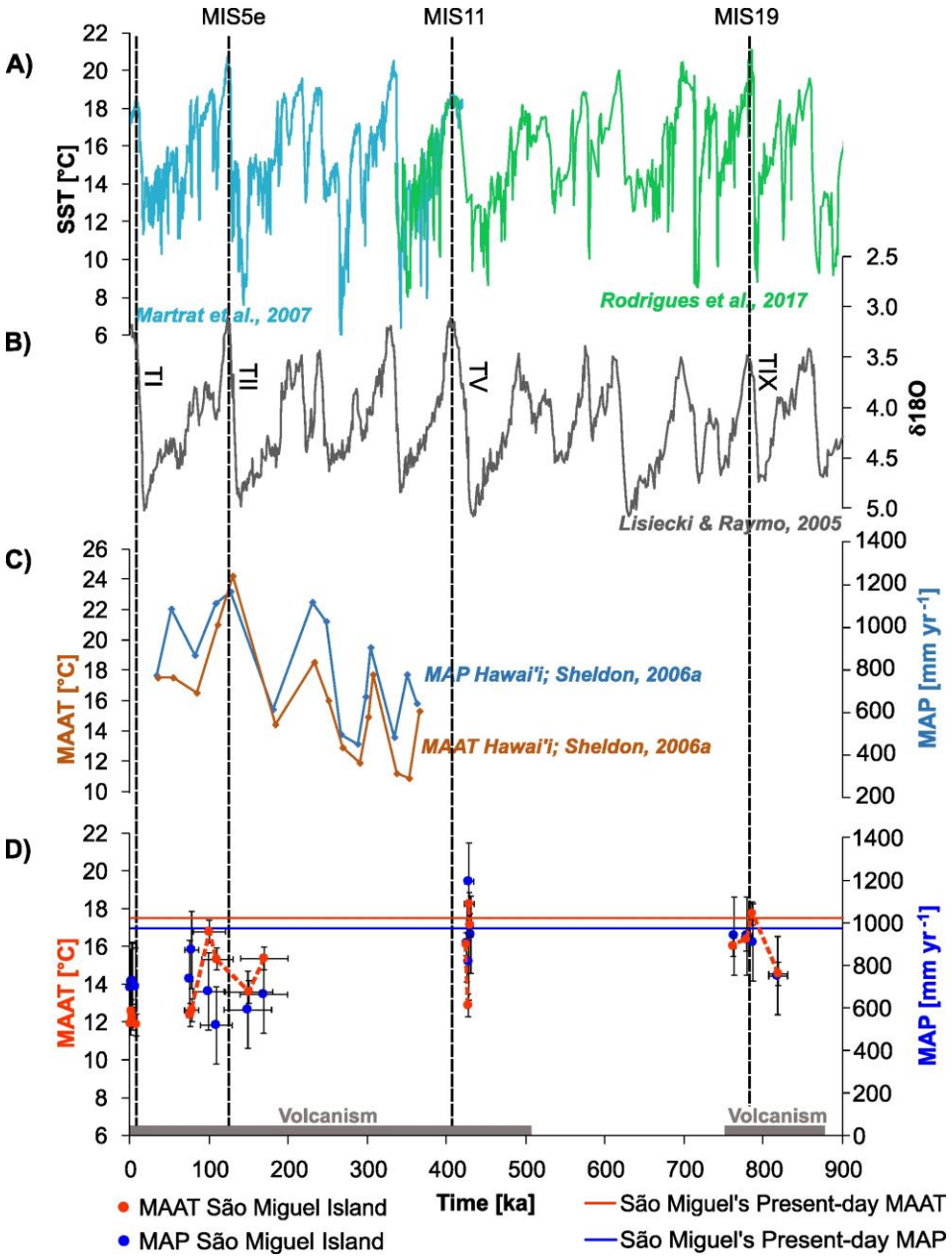

Figure 4: *Climatic reconstructions and comparison with global climatic curves. A) Alkenone-derived Sea Surface Temperature (SST) of the Iberian Margin, sites MD01-2444 for the 420 ka - present period (Martrat et al., 2007), and IODP U1385 for the 1017 ka to 336 ka period (Rodrigues et al., 2017); B) $\delta^{18}O$ of benthic foraminifera (LR04 global stack, Lisiecki and Raymo, 2005); C) MAP and MAAT reconstructions for Hawai'i (Sheldon et al., 2006a); D) The blue circles are our MAP reconstruction based on the CIA-K index, the red circles are our MAAT reconstructions*

based on the Clayeyness index, and the blue and red lines are the current MAP and MAAT at Ponta Delgada, respectively (AEMET & IM, 2012). The PS ages were calculated as in Figure 2 example, and the horizontal error bars represent the maximum soil formation time (see 4.2). The vertical error bars are the standard errors of the methods, which result from the samples and climatic dispersion of the original data set (Sheldon et al., 2002; Sheldon, 2006a). The dashed red line connects the reconstructed MAAT. The gray bar along the horizontal axis shows the main periods of volcanic activity on São Miguel Island (after Sibrant et al., 2015). MIS: Marine Isotope Stage; TI, TII, TV, TIX: Glacial Terminations.

5. Discussion

5.1. Soil formation processes

Most PSs are consistent with equilibrium with the environmental conditions, as indicated by their vertical continuity in the field (no textural changes that could be attributed to sedimentation), limited variations of immobile element ratios, and the up-profile increase of weathering indices (Figure 3; Sheldon and Tabor, 2009), consistent with pedogenesis. In addition, we systematically avoided the upper parts of PSs showing traces of potential surface reworking, thus formation of the PSs here studied was driven by in-situ weathering of volcanic rocks.

Several PSs experienced minor elemental addition (Supplementary Figure SF2), probably associated with ash fall incorporation. Profiles SM21E (site 1), SM21AE (site 11) and SM22H (site 5), which have important variations of immobile elements (e.g., La/Ce) in some horizons, could have incorporated allochthonous materials in their upper horizons. Those materials derived most probably from local explosive volcanism and were quickly weathered and incorporated into the soil, as there is no evidence of sedimentary processes, such as sedimentary structures, or sharp discontinuities and textural changes in the profiles. The high variability in immobile element ratios of profile SM21E (site 1; type III PS dated between ~85 and 71 ka, to the south of Fogo volcano)

449 indicates it was affected by major contamination, probably due to a significant ash fall event, and
450 it was not considered in the paleoclimatic discussion (Supplementary Figure SF2), as its
451 geochemistry is not representative of environmental conditions. The other two cases show
452 evidence of contamination only in their upper part, so their B horizons' geochemistry is probably
453 not affected. The observed Fe accumulation is consistent with pedogenesis under well-aerated
454 conditions.

455 A Ti/Al ratio decrease was observed in several profiles, notably of type I PSs (Figure 3D),
456 which we attribute to the mobility of Ti and relative Al accumulation under high precipitation rates,
457 as previously observed in other settings (e.g., Sheldon and Tabor, 2009; Du et al., 2012).

458 Although the re-sampled profiles were not collected at the exact same depth, they were
459 taken from the same horizons. Weathering indices (e.g., CIA-K) differ by less than 10%. The
460 resulting calculated difference in MAP (~70 mm yr^{-1}) and MAAT (<1 °C) are less than the
461 uncertainties on the proxy relationships. Thus, the replicate analyses indicate minimal
462 heterogeneity within the PS horizons and confirm the robustness of our reconstructions
463 (Supplementary Table ST3).

464 Carbon concentrations in the PSs were generally low, consistent with both well-drained
465 and aerated conditions and modest post-burial oxidation (Sheldon and Tabor, 2009). However,
466 because the $\delta^{13}C$ are virtually all consistent with C_3-dominated ecosystems (e.g., Tipple and
467 Pagani, 2007), it is unlikely that the minor oxidative loss of carbon has substantially altered the
468 PSs' isotopic composition relative to the ecosystem's original composition because C_3-derived
469 organic matter is typically more recalcitrant than C_4-derived organic matter (Wynn, 2007). Thus,
470 we can compare the Pleistocene vegetation to the present-day vegetation. The present-day
471 Azores have only ~4% C_4 plants (about half of which are native; Collins and Jones, 1986) and the
472 PS values all fall within the typical range of Pre-Industrial C_3 plants (-22 to -34‰; Koch, 1998),
473 which suggests relatively little ecosystem-scale upheaval during the Pleistocene despite large-
474 scale climate shifts. Given the relatively isolated position of the Azores (Figure 1), this suggests

instead that the variability of $\delta^{13}C$ through time most likely reflects canopy effects with more negative values corresponding to more closed vegetation (e.g., Cerling and Harris, 1999). As most PSs developed in coastal areas in what are presently similar climatic zones (Figure 1B), we do not expect that geographical differences would have meaningfully impacted the ecosystem composition. Further studies on organic matter in lake cores could elucidate if human activity played a role in the $\delta^{13}C$ variations at human time-scales.

5.2. Textural and lithological control

We note a parent material textural control rather than a compositional control on the formation of PSs, as most of them developed on highly vesicular pyroclastic deposits and the brecciated upper parts of lava flows (Figure 3). Although the upward CIA-K increase is greater in PSs developed in basaltic rocks (type I PSs in Figure 3D), the highest CIA-K (~85) values are reached in a felsic fine-grained ash-fall deposit (type III PS, SM22J of site 5; Supplementary Figure SF2). The higher CIA-K increase of type I PSs can be explained by the lower chemical stability of basaltic rocks compared to the more differentiated ones (e.g., Berner & Kothavala, 2001), and by the higher permeability of pyroclastic deposits, which are parent materials of type II and III PS.

In other volcanic settings, it has been observed that elemental mobility changes rapidly over a precipitation threshold (e.g., Dixon et al., 2016; Bateman et al., 2019). As PSs formed on São Miguel with MAP over ~500 mm yr^{-1} in the case of types II & III PSs, and over ~800 mm yr^{-1} for type I PSs, we suggest that MAP thresholds are different for pyroclastic deposits and lava flows. This difference can be explained by the higher specific surface area of highly-explosive trachytic pyroclastic deposits compared to lava flows and basaltic tephra deposits. This has important consequences regarding the weathering at the island scale: the eastern side of the island is mostly made of massive lava flows, while the central and western parts are primarily covered by pyroclastic deposits (Moore, 1991; Sibrant et al., 2015), and therefore can be more susceptible to weathering. As PS formation is a gradual process, it is probable that those

conditions that exceeded threshold values of precipitation and temperature were sustained for a few thousand years. This is further supported by our geochronological constraints, which typically place maximum soil formation times as < 30,000 years (often much shorter; Supplementary Table ST1), which is a nearly instantaneous process at the timescale of the ten last glacial-interglacial cycles (~1 Ma). Furthermore, Solleiro-Rebolledo et al. (2015) observed that Andisols formed in pyroclastic deposits in less than 10 kyr under MAP values of ~800 mm yr^{-1}. For MAP values of ~4000 mm yr^{-1}, they observed that soil formation is much faster, occurring in less than 500 years. During those periods, surficial (mechanical) erosion also must have been relatively low, permitting the preservation of the soils.

It is important to notice that time does not seem to have played a major role in the weathering degree observed in the different PS profiles. The higher weathering indexes (CIA-K ~80) are reached in two PSs dated between 434±6 ka and 429±6 ka and between 788±11 ka and 776±11 ka (SM22J in site 5 and SM22C in site 3, respectively; Supplementary Table ST1 and Supplementary Figure SF2). In both cases, the maximum and minimum ages are compatible among them considering uncertainties, supporting almost instantaneous (< 30 kyr) pulses of soil formation at the scale of the past 1 Myr. Most of our new geochronological data obtained on volcanic units “bracketing” other PSs are also indistinguishable within uncertainties, reinforcing the fact that weathering occurs fast over only a few kyr and tends to equilibrate quickly (< 20 kyr). Previous work on understanding uncertainties in reconstructing past temperature and precipitation based on PS geochemistry are not time-dependent for PSs with formation times bracketed by the training data set (Sheldon and Tabor, 2009; Tabor and Myers, 2015; Dzombak and Sheldon, 2022).

To summarize, the greater surface area of fine-grained deposits seems to be more important in the weathering kinetics than the geochemistry of the parental rock. Then, differentiated volcanic products might be more susceptible to weathering than less differentiated ones, despite a less reactive geochemistry, because differentiated magmas tend to produce more

527 explosive eruptions. In addition, explosive volcanic products, such as ash, have a great dispersal
528 area and permeability, making the rock-water interactions even more efficient.
529
530 **5.3. Enhanced PS formation during key paleoclimatic transitions**
531 The new ages reported here, along with previously published ages on separated phases
532 (Sibrant et al., 2015; Ricci et al., 2020) provide reliable and tight constraints on the timing of
533 paleosol formation in São Miguel over the last 1 Myr. Typical age uncertainties (few kyr) are
534 comparable with the temporal resolution of global climatic curves, enabling direct and meaningful
535 comparison. Based on these ages, PSs formed during four short periods close to main Marine
536 Isotopic Stages (MIS19, MIS11, MIS5e, Figure 4) supporting pulsed weathering during key
537 climatic transitions. The lack of obvious PS during other periods may be partially explained by the
538 volcanic evolution of the island. For instance, volcanic quiescence between ~750 ka and ~507 ka
539 (Sibrant et al., 2015) precludes age constraints during that time span. This contrasts, for example,
540 with a penecontemporaneous paleosol record from Hawai'i (Figure 4D) that records both more
541 continuous volcanic emplacement and more continuous PS formation. In São Miguel, the absence
542 of PSs in the 765–750 ka, 507–430 ka, 425–170 ka and 75–10 ka periods could further be
543 explained by an accessibility sampling bias, but we note that there are no PSs at those times in
544 cliff face sites either. Instead, São Miguel PS ages are coincident with major global climatic
545 turnovers such as rapid glacial-interglacial transitions when precipitation and temperature evolved
546 rapidly (Figure 4), and, consequently, the initiation of PS formation was probably controlled by
547 paleoclimatic conditions exceeding the local weathering threshold (see *5.2*). The temporal
548 coupling between those pulses of soil formation and glacial terminations supports a significant
549 climatic control on soil-formation processes. Our results suggest that weathering during glacial
550 periods was not efficient enough to produce significant soils, rather than a sampling bias or the
551 loss of soils due to erosion.

552 At least in the context of the PSs observed in São Miguel Island, it seems that the parental
553 rock texture and the climatic forcing are the main factors controlling soil formation processes. As
554 mentioned above (5.2), we observed a clear impact of the parental material on soil formation in
555 response to precipitations, as MAP reconstructions indicate PS formed under dryer conditions in
556 pyroclastic deposits than in lava flows (~500 mm yr^{-1} and ~800 mm yr^{-1}, respectively). The
557 influence of temperature is less evident, but it has also been proposed as a major control of soil
558 formation efficiency, by means of the activation energy for weathering to occur (e.g., Brantley et
559 al., 2023). It is possible that soil-formation processes were not efficient enough during the
560 counterpart of soil-formation pulses because MAP and MAAT thresholds were not surpassed.
561 Some PSs could have been lost due to erosion, but as volcanic gaps do not cover the
562 periods without PSs, we would expect to have found at least some PSs preserved, protected by
563 overriding lava flows. The absence of PSs at higher altitudes can be the result of steeper slopes,
564 which favor erosion, but the PSs studied here were formed in relatively flat lowlands, which are
565 stable even in tropical contexts such as la Reunion Island (e.g., Dosseto et al., 2022). Further
566 campaigns to expand this work, whether to São Miguel Island or other islands of the Azores, could
567 help to elucidate if the lack of PS over those periods reflects a sampling bias, and eventually fill
568 temporal gaps. According to our results, we could expect to find PSs developed near other glacial
569 terminations.
570 The PSs of the 425–430 ka age group indicate a particularly high increase of MAP in the
571 northern side of the island (~940 to ~1200 mm yr^{-1}) and of MAAT in the southern coast (~13 to
572 ~16 °C) relative to the glacial baseline, probably recording the fast climatic change of the glacial-
573 interglacial transition after Termination V, which amplitude is comparable to Termination I (Figure
574 4E; Lang and Wolff, 2011). The two other major periods of paleosol formation are each centered
575 on MIS 19 and 5e, respectively, and also record major local climate changes (Figure 4E).
576 Enhanced soil formation can have impacts at different temporal and spatial scales (Dzombak and
577 Sheldon, 2020), such as changes in soil fertility and production (Melo et al., 2022), and global

carbon cycling due to the atmospheric CO_2 consumption through weathering (Dessert et al., 2003). The consequent clay increase in the substrate can alter the mechanical response to hydration, eventually promoting minor landslides, which needs to be further studied. These and other possible impacts of paleoclimatic changes are of great scientific and societal interest, especially under the actual context of global warming and fast climatic changes.

5.4. Local climate as a function of global climate

Our tight temporal constraints in the two older age-groups, and in some PSs of the younger ones, allow us to compare our local paleoclimatic reconstruction directly with global climatic conditions from other proxy records. The new results are consistent with colder and dryer conditions during glacial periods, and warmer and wetter conditions during interglacial periods, as in most global records (Figure 4A, C), with the highest MAP and MAAT values during interglacial peaks (MIS19, MIS11 and MIS5e-a). Glacial Termination II and IX are both defined by rising and then falling MAAT. It is challenging to unravel the spatial paleoclimate variation across the island, as parent material, global climate, altitude, and timing are also different. All PSs were collected near coastal areas, so altitude should not be an issue, but the location with respect to wind direction should have an impact on MAPs. Most PSs developed in what are today Csb climatic zones (temperate with dry-warm summer). SM22E (site 4) is in the limit with Cfb (temperate no dry season with mild summer) so different climatic zones should not have triggered great differences, assuming the present climatic zones were the same in the past. The exception is SM21S (site 6, northern shore), in a Cfa climatic zone (temperate no dry season with hot summer), for which MAP and MAAT (~730 mm yr^{-1}; 12.4 °C) were lower than SM21A (site 1; ~870 mm yr^{-1}; 12.6 °C; the southern shore) in a Csb climatic zone (temperate with dry-warm summer), with comparable age. This could record different past climatic zones distribution, nevertheless, MAP and MAAT are compatible between the two profiles within uncertainties. In contrast, PSs developed in the 425–430 ka age group recorded significantly wetter and warmer conditions on

604 the northern side of the island compared to the south (~800–900 mm yr^{-1} and ~13–16 °C on the
605 southern shore, and 940–1200 mm yr^{-1} and ~17–18 °C on the northern shore). Currently, the
606 northern part of the island is also wetter and warmer, which suggests that other meteorological
607 factors (e.g., wind direction) were similar in the Pleistocene even as the absolute conditions were
608 less equable.

609 Within age error, the warmest paleotemperatures recorded on São Miguel correspond to
610 Sea Surface Temperature (SST) peaks in the North Atlantic (Figure 4B). This suggests that the
611 local climate is largely controlled by the broader global climatic forcings that drove climate of the
612 northern hemisphere during the Pleistocene. A possible consequence of this teleconnection is the
613 moderately dryer paleoprecipitation estimates over much of the past 800 kyr relative to present
614 conditions, which might be the result of extended periods of ice sheet accumulation during glacial
615 periods. The absolute magnitude of temperature change is slightly smaller than for SST during
616 the glacial-interglacial conditions, and much smaller than for a penecontemporaneous paleosol
617 record in Hawai'i. A possible explanation for this discrepancy is that Mauna Loa and Mauna Kea
618 volcanoes had much higher elevations (>3000 m) than any of the volcanoes on São Miguel (<1200
619 m), leading to the amplification of local climatic differences. This is supported by the observation
620 that the Hawaiian volcanoes were tall enough to form localized glaciers and moraines (Porter,
621 2005) even when the low-elevation paleosol-derived paleotemperatures were similar to Pacific
622 sub-tropical SSTs (Sheldon, 2006a).
623

624 **6. Conclusions**

625 São Miguel, in the Eastern Azores, provides a natural laboratory for understanding how
626 Quaternary glacial-interglacial climate changes have driven weathering on volcanic islands.
627 Precise new ages on volcanic products can be used to bracket the age of PSs and to determine
628 the duration of PS formation. The low uncertainties of the geochronological methods used here
629 and the tight temporal constraint of PS formation time allow a direct comparison with global

conditions during key climatic transitions. The formation of paleosols in São Miguel is a function of both the texture (rather than chemistry) of the volcanic parent materials and the evolution of local environmental conditions. The formation of PSs on pyroclastic deposits and lava flows at different precipitation thresholds emphasizes the importance of primary volcanic fragmentation in the PS formation process.

Overall, São Miguel's paleosols typically formed in pulses during major global climatic transitions, and gaps in the record reflect periods of volcanic quiescence and relatively dry and cold conditions. Pleistocene MAAT and MAP estimates are typically modestly cooler and drier than present conditions, but also show a clear difference between cool/dry glacial and warm/wet interglacial periods that match global climatic conditions. Warmer and wetter intervals in the past also seem to correlate with periods of enhanced weathering, suggesting that future climate change may result in enhanced weathering in the Azores and other volcanic islands.

Acknowledgements

This work was supported by the CNRS-INSU TelluS-SYSTER program 2022-2023. F.H-C. especially acknowledges the French MESRI doctoral program (2020-2023). We thank two anonymous reviewers, whose comments greatly helped to improve this work. We also thank Tomas Martinez for his valuable support in the field, Sebastien Nomade and Alison Pereira for their help with $^{40}Ar/^{39}Ar$ analyses, Gaël Monvoisin for his help regarding sample leaching for geochemical analyses, Valerie Godard for thin section preparation, and X. Quidelleur for his careful reading of the manuscript. This is LGMT contribution number 187.

References

1. AEMET & IM (2012) Atlas Climático de los Archipiélagos de Canarias, Madeira y Azores. Agencia Estatal de Meteorología de España e Instituto de Meteorología de Portugal. https://doi.org/10.31978/281-12-006-X

2. Bateman, J. B., Chadwick, O. A., Vitousek, P. M. (2019) Quantitative analysis of pedogenic thresholds and domains in volcanic soils. Ecosystems, 22(7), 1633-1649. https://doi.org/10.1007/s10021-019-00361-1

3. Berner, R. A., & Kothavala, Z. (2001) GEOCARB III: a revised model of atmospheric CO2 over Phanerozoic time. American Journal of Science, 301(2), 182-204. https://doi.org/10.2475/ajs.301.2.182

4. Börker, J., Hartmann, J., Romero-Mujalli, G., Li, G. (2019) Aging of basalt volcanic systems and decreasing CO2 consumption by weathering. Earth Surface Dynamics, 7(1), 191-197. https://doi.org/10.5194/esurf-7-191-2019

5. Carmichael, R. S. (2017) Practical handbook of physical properties of rocks and minerals (1988). CRC press. https://doi.org/10.1201/9780203710968

6. Cerling, T. C., & Harris, J. M. (1999) Carbon isotope fractionation between diet and bioapatite in ungulate mammals and implications for ecological and paleoecological studies. Oecologia 120, 347-363. https://doi.org/10.1007/s004420050868

7. Chadwick, O. A., Brimhall, G. H., Hendricks, D. M. (1990) From a black to a gray box—a mass balance interpretation of pedogenesis. Geomorphology, 3(3-4), 369-390. https://doi.org/10.1016/0169-555X(90)90012-F

8. Chadwick, O. A., Chorover, J., Chadwick, K. D., Bateman, J. B., Slessarev, E. W., Kramer, M., Thompson, A., Vitousek, P. M. (2022) Constraints of climate and age on soil development in Hawai ‘i. In Biogeochemistry of the Critical Zone (pp. 49-88). Cham: Springer International Publishing. https://doi.org/10.1007/978-3-030-95921-0_3

9. Collins, R. P., & Jones, M. B. (1986) The influence of climatic factors on the distribution of C_4 plant in Europe. Vegetation 64, 121-129. https://doi.org/10.1007/BF00044788

10. Conte, E., Widom, E., Kuentz, D., França, Z. (2019) 14C and U-series disequilibria age constraints from recent eruptions at Sete Cidades volcano, Azores. Journal of Volcanology and Geothermal Research, 373, 167-178. https://www.doi.org/10.1016/j.jvolgeores.2019.02.002

11. Cresswell-Clay, N., Ummenhofer, C. C., Thatcher, D. L., Wanamaker, A. D., Denniston, R. F., Asmerom, Y., Polyak, V. J. (2022) Twentieth-century Azores High expansion unprecedented in the past 1,200 years. Nature Geoscience, 15(7), 548-553. https://doi.org/10.1038/s41561-022-00971-w

12. De la Horra, R., Galán-Abellán, A. B., López-Gómez, J., Sheldon, N. D., Barrenechea, J. F., Luque, F. J., Arche, Benito, M. I. (2012) Paleoecological and paleoenvironmental changes during the continental Middle–Late Permian transition at the SE Iberian Ranges, Spain. Global and Planetary Change, 94, 46-61. https://doi.org/10.1016/j.gloplacha.2012.06.008

13. Dessert, C., Dupré, B., Gaillardet, J., François, L. M., Allègre, C. J. (2003) Basalt weathering laws and the impact of basalt weathering on the global carbon cycle. Chemical Geology, 202(3-4), 257-273. https://doi.org/10.1016/j.chemgeo.2002.10.001

14. Dixon, J. L., Chadwick, O. A., Vitousek, P. M. (2016) Climate-driven thresholds for chemical weathering in postglacial soils of New Zealand. Journal of Geophysical Research: Earth Surface, 121(9), 1619-1634. https://doi.org/10.1002/2016JF003864

15. Du, X., Rate, A. W., Gee, M. M. (2012) Redistribution and mobilization of titanium, zirconium and thorium in an intensely weathered lateritic profile in Western Australia. Chemical Geology, 330, 101-115. https://doi.org/10.1016/j.chemgeo.2012.08.030

16. Dzombak, R. M., & Sheldon, N. D. (2020) Weathering intensity and presence of vegetation are key controls on phosphorus concentrations: implications for past and future terrestrial ecosystems. Soil Systems, 4(4), 73. https://doi.org/10.3390/soilsystems4040073

17. Dzombak, R. M., & Sheldon, N. D. (2022) Terrestrial records of weathering indicate three billion years of dynamic equilibrium. Gondwana Research, 109, 376-393. https://doi.org/10.1016/j.gr.2022.05.009

18. Giaccio, B., Marino, G., Marra, F., Monaco, L., Pereira, A., Zanchetta, G., Gaeta, M., Leicher, N., Nomade, S., Palladino, D. M., Sottili, G., Guillou, H., Scao, V. (2021) Tephrochronological constraints on the timing and nature of sea-level change prior to and during glacial termination V. Quaternary Science Reviews, 263, 106976. https://doi.org/10.1016/j.quascirev.2021.106976

19. Gillot, P., & Cornette, Y. (1986) The Cassignol technique for potassium—Argon dating, precision and accuracy: Examples from the Late Pleistocene to Recent volcanics from southern Italy. Chemical Geology: Isotope Geoscience section, 59, 205-222. https://doi.org/10.1016/0168-9622(86)90072-2

20. Gillot, P.Y., Cornette, Y., Max, N., Floris, B. (1992) Two reference materials, trachytes MDO-G and ISH-G, for argon dating (K-Ar and 40Ar/39Ar) of Pleistocene and Holocene rocks. Geostandards Newsletter, 16(1), 55-60. https://doi.org/10.1111/j.1751-908X.1992.tb00487.x

21. Gillot, P., Albore-Livadie, C., Lefèvre, J., Hildebrand, A. (2006) The K/Ar dating method: principle, analytical techniques, and application to Holocene volcanic eruptions in southern Italy. The K/Ar Dating Method, 1000-1011.

22. Hernández, A., Kutiel, H., Trigo, R., Valente, M., Sigró, J., Cropper, T., Santo, E. (2016) New Azores archipelago daily precipitation dataset and its links with large-scale modes of climate variability. International Journal of Climatology, 36(14), 4439-4454. https://doi.org/10.1002/joc.4642

23. Hildenbrand, A., Gillot, P., Marlin, C. (2008a) Geomorphological study of long-term erosion on a tropical volcanic ocean island: Tahiti-Nui (French Polynesia). Geomorphology, 93(3-4), 460-481. https://doi.org/10.1016/j.geomorph.2007.03.012

728 24. Hildenbrand, A., Madureira, P., Marques, F. O., Cruz, I., Henry, B., Silva, P. (2008b) Multi-
729 stage evolution of a sub-aerial volcanic ridge over the last 1.3 Myr: S. Jorge Island, Azores Triple
730 Junction. Earth and Planetary Science Letters, 273(3-4), 289-298.
731 http://dx.doi.org/10.1016/j.epsl.2008.06.041
732 25. Hildenbrand, A., Marques, F. O., Costa, A. C. G., Sibrant, A. L. R., Silva, P. F., Henry, B.,
733 Mirande, J. M., Madureira, P. (2012) Reconstructing the architectural evolution of volcanic islands
734 from combined K/Ar, morphologic, tectonic, and magnetic data: The Faial Island example
735 (Azores). Journal of Volcanology and Geothermal Research, 241, 39-48.
736 https://doi.org/10.1016/j.jvolgeores.2012.06.019
737 26. Hildenbrand, A., Weis, D., Madureira, P., Marques, F. O. (2014) Recent plate re-
738 organization at the Azores Triple Junction: evidence from combined geochemical and
739 geochronological data on Faial, S. Jorge and Terceira volcanic islands. Lithos, 210, 27-39.
740 https://doi.org/10.1016/j.lithos.2014.09.009
741 27. Hildenbrand, A., Marques, F. O., Catalão, J. (2018) Large-scale mass wasting on small
742 volcanic islands revealed by the study of Flores Island (Azores). Scientific Reports, 8(1), 13898.
743 https://doi.org/10.1038/s41598-018-32253-0
744 28. Johnson, C. L., Wijbrans, J. R., Constable, C. G., Gee, J., Staudigel, H., Tauxe, L., Forjaz,
745 V. H., Salguerio, M. (1998). $^{40}Ar/^{39}Ar$ ages and paleomagnetism of São Miguel lavas, Azores.
746 Earth and Planetary Science Letters. 160, 637–649. https://doi.org/10.1016/s0012-
747 821x(98)00117-4
748 29. Klein, B., & Siedler, G. (1989) On the origin of the Azores Current. Journal of Geophysical
749 Research: Oceans, 94(C5), 6159-6168. https://doi.org/10.1029/JC094iC05p06159
750 30. Koch, P. L. (1998) Isotopic reconstruction of past terrestrial environments. Annual Reviews
751 of Earth and Planetary Sciences, 26, 573-613. https://doi.org/10.1146/annurev.earth.26.1.573
752 31. Köppen, W. (1936) Das geographische System de Klimate. Handbuch der klimatologie,
753 band I, teil C. Edited by Köppen, W. and Geiger. Berlin.

754 32. Koppers, A. A. (2002) ArArCALC—software for 40Ar/39Ar age calculations. Computers &
755 Geosciences, 28(5), 605-619. http://dx.doi.org/10.1016/S0098-3004(01)00095-4
756 33. Kramer, M. G. & Chadwick, O. A. (2016) Controls on carbon storage and weathering in
757 volcanic soils across a high-elevation climate gradient on Mauna Kea, Hawaii. Ecology, 97(9),
758 2384-2395. https://doi.org/10.1002/ecy.1467
759 34. Lang, N., & Wolff, E. W. (2011) Interglacial and glacial variability from the last 800 ka in
760 marine, ice and terrestrial archives. Climate of the Past, 7(2), 361-380. https://doi.org/10.5194/cp-
761 7-361-2011
762 35. Le Bas, M. J., Le Maitre, R. W., Streckeisen, A., Zanettin, B., IUGS Subcommission on the
763 Systematics of Igneous Rocks (1986) A chemical classification of volcanic rocks based on the
764 total alkali-silica diagram. Journal of Petrology, 27(3), 745-750.
765 https://doi.org/10.1093/petrology/27.3.745
766 36. Lee, J. Y., Marti, K., Severinghaus, J. P., Kawamura, K., Yoo, H. S., Lee, J. B., Kim, J. S.
767 (2006) A redetermination of the isotopic abundances of atmospheric Ar. Geochimica et
768 Cosmochimica Acta, 70(17), 4507-4512. http://dx.doi.org/10.1016/j.gca.2006.06.1563
769 37. Lisiecki, L. & Raymo, M. (2005) A Pliocene-Pleistocene stack of 57 globally distributed
770 benthic δ18O records. Paleoceanography, 20(1). https://doi.org/10.1029/2004PA001071
771 38. Mack, G., James, W., Monger, H. (1993) Classification of paleosols. Geological Society of
772 America Bulletin, 105(2), 129-136. https://doi.org/10.1130/0016-
773 7606(1993)105%3C0129:COP%3E2.3.CO;2
774 39. Marbut, C. F. (1935) Atlas of American agriculture. III. Soils of the United States.
775 Washington, D.C., Government Printing Office.
776 40. Marques, F., Catalão, J., DeMets, C., Costa, A., Hildenbrand, A. (2013) GPS and tectonic
777 evidence for a diffuse plate boundary at the Azores Triple Junction. Earth and Planetary Science
778 Letters, 381, 177-187. https://doi.org/10.1016/j.epsl.2013.08.051

779 41. Marques, F. O., Hildenbrand, A., Hübscher, C. (2018) Evolution of a volcanic island on the
780 shoulder of an oceanic rift and geodynamic implications: S. Jorge Island on the Terceira Rift,
781 Azores Triple Junction. Tectonophysics, 738, 41-50. https://doi.org/10.1016/j.tecto.2018.05.012
782 42. Martrat, B., Grimalt, J. O., Shackleton, N. J., de Abreu, L., Hutterli, M. A., Stocker, T. F.
783 (2007) Four climate cycles of recurring deep and surface water destabilizations on the Iberian
784 margin. Science, 317(5837), 502-507. https://doi.org/10.1126/science.1139994
785 43. Maynard, J. (1992) Chemistry of modern soils as a guide to interpreting Precambrian
786 paleosols. The Journal of Geology. 100 (3), 279–289. https://doi.org/10.1086/629632
787 44. Melo, C. D., Maduro Dias, C. S., Wallon, S., Borba, A. E., Madruga, J., Borges, P. A.,
788 Ferreira, M. T., Elias, R. B. (2022) Influence of climate variability and soil fertility on the forage
789 quality and productivity in Azorean pastures. Agriculture, 12(3), 358.
790 https://doi.org/10.3390/agriculture12030358
791 45. Menviel, L., Capron, E., Ivanovic, R. (2020) Glacial terminations: Processes and
792 feedbacks. Past Global Changes PAGES Magazine, 29(1), 56, 2021.
793 https://doi.org/10.22498/pages.29.1.56
794 46. Milne, J. D. G., Clayden, B., Singleton, P. L., Wilson, A. D. (1995) Soil Description
795 Handbook. Manaaki Whenua Press, Lincoln, 157 pp.
796 47. Monaco, L., Leicher, N., Palladino, D. M., Arienzo, I., Marra, F., Petrelli, M., Nomade, S.,
797 Pereira, A., Sottili, G., Conticelli, S., D'Antonio, M., Fabbrizio, A., Jicha, B. R., Mannella, G.,
798 Petrosino, P., Ragattieri, E., Tzedakis, P. C., Wagner, B., Zanchetta, G., Giaccio, B. (2022) The
799 Fucino 250–170 ka tephra record: New insights on peri-Tyrrhenian explosive volcanism, central
800 mediterranean tephrochronology, and timing of the MIS 8-6 climate variability. Quaternary
801 Science Reviews, 296, 107797. https://doi.org/10.1016/j.quascirev.2022.107797
802 48. Moore, R. B. (1991). Geologic map of São Miguel, Azores. USGS, series No. 2007.
803 https://doi.org/10.3133/i2007

804 49. Moore, J. G. (2001) Density of basalt core from Hilo drill hole, Hawaii. Journal of
805 Volcanology and Geothermal Research, 112(1-4), 221-230. https://doi.org/10.1016/S0377-
806 0273(01)00242-6
807 50. Niespolo, E. M., Rutte, D., Deino, A. L., Renne, P. R. (2017) Intercalibration and age of
808 the Alder Creek sanidine 40Ar/39Ar standard. Quaternary Geochronology, 39, 205-213.
809 https://doi.org/10.1016/j.quageo.2016.09.004
810 51. Orr, T. J., Roberts, E. M., Wurster, C. M., Mtelela, C., Stevens, N. J., O'connor, P. M.
811 (2021) Paleoclimate and paleoenvironment reconstruction of paleosols spanning the Lower to
812 Upper Cretaceous from the Rukwa Rift Basin, Tanzania. Palaeogeography, Palaeoclimatology,
813 Palaeoecology, 577, 110539. https://doi.org/10.1016/j.palaeo.2021.110539
814 52. Pereira, A., Monaco, L., Marra, F., Nomade, S., Gaeta, M., Leicher, N., Palladino, D. M.,
815 Sottili, G., Guillou, H., Scao, V, Giaccio, B. (2020) Tephrochronology of the central Mediterranean
816 MIS 11c interglacial (~ 425–395 ka): New constraints from the Vico volcano and Tiber delta,
817 central Italy. Quaternary Science Reviews, 243, 106470.
818 https://doi.org/10.1016/j.quascirev.2020.106470
819 53. Polacci, M., Pioli, L., Rosi, M. (2003) The Plinian phase of the Campanian Ignimbrite
820 eruption (Phlegrean Fields, Italy): evidence from density measurements and textural
821 characterization of pumice. Bulletin of Volcanology, 65, 418-432. https://doi.org/10.1007/s00445-
822 002-0268-4
823 54. Porter, S. C. (2005) Pleistocene snowlines and glaciation of the Hawaiian Islands.
824 Quaternary International, 138-139, 118-128. https://doi.org/10.1016/j.quaint.2005.02.009
825 55. Quidelleur, X., Michon, L., Famin, V., Geffray, M. C., Danišík, M., Gardiner, N., Rusquet,
826 A., Zakaria, M. G. (2022) Holocene volcanic activity in Anjouan Island (Comoros archipelago)
827 revealed by new Cassignol-Gillot groundmass K–Ar and 14C ages. Quaternary Geochronology,
828 67, 101236. http://dx.doi.org/10.1016/j.quageo.2021.101236

56. Rad, S., Cerdan, O., Rivé, K., Grandjean, G. (2011) Age of river basins in Guadeloupe impacting chemical weathering rates and land use. Applied Geochemistry, 26, S123-S126. https://doi.org/10.1016/j.apgeochem.2011.03.046

57. Rad, S., Rivé, K., Vittecoq, B., Cerdan, O., Allègre, C. J. (2013) Chemical weathering and erosion rates in the Lesser Antilles: An overview in Guadeloupe, Martinique and Dominica. Journal of South American Earth Sciences, 45, 331-344. https://doi.org/10.1016/j.jsames.2013.03.004

58. Rashid, S. A., Iqbal, M. J., Hussain, M. A. (2012) Impact of north-south shift of Azores High on summer precipitation over North West Europe. International Journal of Geosciences, 3(05), 992-999. http://dx.doi.org/10.4236/ijg.2012.325099

59. Renne, P. R., Swisher, C. C., Deino, A. L., Karner, D. B., Owens, T. L., DePaolo, D. J. (1998) Intercalibration of standards, absolute ages and uncertainties in 40Ar/39Ar dating. Chemical Geology, 145(1-2), 117-152. https://doi.org/10.1016/S0009-2541(97)00159-9

60. Renne, P. R., Balco, G., Ludwig, K. R., Mundil, R., & Min, K. (2011) Response to the comment by WH Schwarz et al. on "Joint determination of 40K decay constants and 40Ar∗/40K for the Fish Canyon sanidine standard, and improved accuracy for 40Ar/39Ar geochronology" by PR Renne et al. (2010). Geochimica et Cosmochimica Acta, 75(17), 5097-5100. https://doi.org/10.1016/j.gca.2011.06.021

61. Retallack, G. (2001) Soils of the past: an introduction to paleopedology (2nd ed). London, Blackwell Science, 404 p.

62. Ricci, J., Carlut, J., Marques, F. O., Hildenbrand, A., Valet, J. P. (2020) Volcanic record of the last geomagnetic reversal in a lava flow sequence from the Azores. Frontiers in Earth Science, 8, 165. https://doi.org/10.3389/feart.2020.00165

63. Rodrigues, T., Alonso-García, M., Hodell, D. A., Rufino, M., Naughton, F., Grimalt, J. O., Voelker, H.A.L., Abrantes, F. (2017) A 1-Ma record of sea surface temperature and extreme cooling events in the North Atlantic: A perspective from the Iberian Margin. Quaternary Science Reviews, 172, 118-130. https://doi.org/10.1016/j.quascirev.2017.07.004

855 64. Rosi, M., Vezzoli, L., Castelmenzano, A., Grieco, G. (1999) Plinian pumice fall deposit of
856 the Campanian Ignimbrite eruption (Phlegraean Fields, Italy). Journal of Volcanology and
857 Geothermal Research, 91(2-4), 179-198. https://doi.org/10.1016/S0377-0273(99)00035-9
858 65. Schwarz, W. H., & Trieloff, M. (2007) Intercalibration of 40Ar–39Ar age standards NL-25,
859 HB3gr hornblende, GA1550, SB-3, HD-B1 biotite and BMus/2 muscovite. Chemical Geology,
860 242(1-2), 218-231.
861 66. Sheldon, N. D., & Retallack, G. J. (2001) Equation for compaction of paleosols due to
862 burial. Geology, 29(3), 247-250. https://doi.org/10.1130/0091-
863 7613(2001)029%3C0247:EFCOPD%3E2.0.CO;2
864 67. Sheldon, N. D., Retallack, G., Tanaka, S. (2002) Geochemical climofunctions from North
865 American soils and application to paleosols across the Eocene-Oligocene boundary in Oregon.
866 The Journal of Geology, 110(6), 687-696. http://dx.doi.org/10.1086/342865
867 68. Sheldon, N. D. (2003) Pedogenesis and geochemical alteration of the Picture Gorge
868 Subgroup, Columbia River Basalt, Oregon. Geological Society of America Bulletin, 115, 1377-
869 1387. https://doi.org/10.1130/B25223.1
870 69. Sheldon, N. D. (2006a) Quaternary glacial-interglacial climate cycles in Hawaii. The
871 Journal of Geology, 114(3), 367-376. http://dx.doi.org/10.1086/500993
872 70. Sheldon, N. D. (2006b) Using paleosols of the Picture Gorge Basalt to reconstruct the
873 middle Miocene climatic optimum. PaleoBios, 26(2), 27–36.
874 71. Sheldon, N. D. & Tabor, N. (2009) Quantitative paleoenvironmental and paleoclimatic
875 reconstruction using paleosols. Earth-science reviews, 95(1-2), 1-52.
876 https://doi.org/10.1016/j.earscirev.2009.03.004
877 72. Sibrant, A., Hildenbrand, A., Marques F., Weiss, B., Boulesteix, T., Hübscher, C.,
878 Lüdmann, T., Costa, A., Catalão, J. (2015) Morpho-structural evolution of a volcanic island
879 developed inside an active oceanic rift: S. Miguel Island (Terceira Rift, Azores). Journal of

880 Volcanology and Geothermal Research, 301, 90-106.
881 https://doi.org/10.1016/j.jvolgeores.2015.04.011
882 73. Sibrant, A. L. R., Marques, F. O., Hildenbrand, A., Boulesteix, T., Costa, A. C. G., Catalão,
883 J. (2016) Deformation in a hyperslow oceanic rift: Insights from the tectonics of the São Miguel
884 Island (Terceira Rift, Azores). Tectonics, 35(2), 425-446. https://doi.org/10.1002/2015TC003886
885 74. Soil Survey Staff (2014) Keys to Soil Taxonomy, 12th edition. USDA-Natural Resources
886 Conservation Service, Washington, DC.
887 75. Solleiro-Rebolledo, E., Sedov, S., Cabadas-Báez, H. (2015) Use of soils and palaeosols
888 on volcanic materials to establish the duration of soil formation at different chronological scales.
889 Quaternary International, 376, 5-18. https://doi.org/10.1016/j.quaint.2014.12.002
890 76. Sowards, K. F., Nelson, S. T., McBride, J. H., Bickmore, B. R., Heizler, M. T., Tingey, D.
891 D., Rey, K. A., Yaede, J. R. (2018) A conceptual model for the rapid weathering of tropical ocean
892 islands: A synthesis of geochemistry and geophysics, Kohala Peninsula, Hawaii, USA.
893 Geosphere, 14(3), 1324-1342. https://doi.org/10.1130/GES01642.1
894 77. Steinhilber, F., Abreu, J. A., Beer, J., Brunner, I., Christl, M., Fischer, H., Heikkilä, U.,
895 Kubik, P. W., Mann, M., McCracken, K. G., Miller, H., Miyahara, H., Oerter, H., Wilhelms, F. (2012)
896 9,400 years of cosmic radiation and solar activity from ice cores and tree rings. Proceedings of
897 the National Academy of Sciences, 109(16), 5967-5971.
898 https://doi.org/10.1073/pnas.1118965109
899 78. Steiger, R. H., & Jäger, E. (1977) Subcommission on geochronology: convention on the
900 use of decay constants in geo-and cosmochronology. Earth and Planetary Science Letters, 36(3),
901 359-362. https://doi.org/10.1016/0012-821X(77)90060-7
902 79. Tabor, N. J., & Myers, T. S. (2015) Paleosols as indicators of paleoenvironment and
903 paleoclimate. Annual Review of Earth and Planetary Sciences, 43, 333-361.
904 https://doi.org/10.1146/annurev-earth-060614-105355

905 80. Thatcher, D. L., Wanamaker, A. D., Denniston, R. F., Ummenhofer, C. C., Regala, F. T.,
906 Jorge, N., Haws, J., Chormann, A., Gillikin, D. P. (2020) Linking the karst record to atmospheric,
907 precipitation, and vegetation dynamics in Portugal. Chemical Geology, 558, 119949.
908 https://doi.org/10.1016/j.chemgeo.2020.119949
909 81. Tipple, B. J., & Pagani, M. (2007) The early origins of terrestrial C_4 photosynthesis. Annual
910 Reviews of Earth and Planetary Science Letters 35, 435-461.
911 http://dx.doi.org/10.1146/annurev.earth.35.031306.140150
912 82. White, R. E. (2005) Principles and practice of soil science: the soil as a natural resource.
913 John Wiley & Sons.
914 83. Wilson, S. A. (1997) The collection, preparation and testing of USGS reference material
915 BCR-2, Columbia River Basalt: US Geological Survey Open-File Report.
916 84. Wynn, J. G. (2007) Carbon isotope fractionation during decomposition of organic matter
917 in soils and paleosols: implications for paleoecological interpretations of paleosols.
918 Palaeogeography, Palaeoclimatology, Palaeoecology, 251(3-4), 437-448.
919 https://doi.org/10.1016/j.palaeo.2007.04.009